MIT Department of Nuclear Engineering

Measurement of near-surface void fraction and macrolayer thickness in boiling water and silica-based nanofluid

by
Andrew Lerch

SUBMITTED TO THE DEPARTMENT OF NUCLEAR SCIENCE
AND ENGINEERING
IN PARTIAL FULFILLMENT OF THE REQUIREMENTS FOR THE DEGREE OF

BACHELOR OF SCIENCE IN NUCLEAR SCIENCE AND ENGINEERING
AT THE
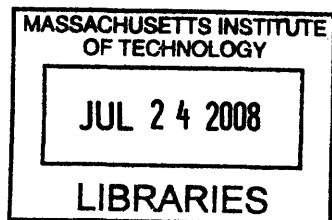MASSACHUSETTS INSTITUTE OF TECHNOLOGY
[June 2008]
MAY 2008

Author: ....
Andrew J. Lerch, Nuclear Science and Engineering
May 9, 2008

Approved by: ....
Thesis Supervisor, Prof. Jacopo Buongiorno

Approved by: ....
Thesis Co-Supervisor, Dr. Lin-Wen Hu

Approved by: ....
Chairman, Undergraduate Thesis Committee, Prof. David Cory

Measurement of near-surface void fraction and macrolayer thickness in boiling water and silica-based nanofluid
by
Andrew Lerch

Submitted to the Department of Nuclear Science and Engineering on May 9, 2008
In Partial Fulfillment of the Requirements for the Degree of
Bachelor of Science in Nuclear Science and Engineering

ABSTRACT

Nanofluids are engineered fluids that contain a suspension of nanoparticles in a pure substance. Nanoparticles can be any variety of metals, metal oxides, or ceramics. They have been shown to increase heat transfer properties such as thermal conductivity, convective heat transfer, and critical heat flux (CHF). An optical probe used to detect phase was used to measure the void fraction during boiling, from which the macrolayer thickness can be derived. The optical probe was verified to have an error of 11.9% and 10.4% for measuring bubble diameter in water and R-123, respectively, and an error of 5.2% and 7.1% for measuring velocity in water and R-123. The macrolayer dryout theory of CHF was tested by investigating the change in macrolayer thickness for different heat fluxes in de-ionized (DI) water and 0.01% (by volume) SiO_2 nanofluid. A current controlled power source heated a sandblasted, stainless steel plate resting in an isothermal bath. The silica nanofluid had a CHF enhancement of 82% over the DI water along with a slightly higher (20% enhancement) heat transfer coefficient. The macrolayer thickness, as measured by the optical probe, at a comparable heat flux was much larger than the DI water, possibly due to the increased wettability of the heater caused by the deposition of nanoparticles on the heater. This trend is in agreement with prediction of existing theory.

Thesis Supervisor: Jacopo Buongiorno
Title: Assistant Professor

Thesis Co-supervisor: Lin-Wen Hu
Title: Associate Director, Research Dev & Utilization – MIT Nuclear Reactor Lab

Table of Contents

Figures

Tables

Nomenclature:

A	Area (m^2)
c	Constant to determine nucleation site density
C	Constant in Zuber relation
d	Diameter (m)
Eo	Eotvos Number
f	Frequency of departure (s^{-1})
g	Acceleration due to gravity (m/s^2)
h	Heat Transfer Coefficient (W/m^2 °C)
I	Current (A)
k	Thermal Conductivity (W/m °C)
l	Length (m)
$\dot{m}$	Mass flow rate (kg/s)
Mo	Morton Number
n	Index of Refraction
N	Nucleation site density
ΔP	Pressure loss (Pa)
$q"$	Heat flux (W/m^2)]
r	Radius of bubble (m)
Re	Reynolds Number
T	Temperature (°C)
U	Velocity (m/s)
v	Velocity (m/s)
V	Voltage (V)
w	Width (m)

w	wall
v	vapor

Abbreviations:

CHF	Critical Heat Flux
DAQ	Data Acquisition System
ISO	Interface Software for Optical Probe
$LOCA$	Loss of Cooling Accident
OP	Optical Probe
PBE	Pool Boiling Experiment
PWR	Pressurized Water Reactor

Greek Symbols:

δ	Macrolayer Thickness(m)
μ	Viscosity (Pa*s)
ν	Wavenumber (s^{-1})
ρ	density (kg/m^3)
σ	surface tension (N/m)
φ	Nanoparticle volume fraction (%)
τ	Dryout time (s)

Subscript:

b	Bulk
c	Cross section
d	Dryout
e	Equivalent
f	Fluid
g	Gas
inj	Air Injector
h	Heater
l	Liquid

1 Introduction

1.1 Gen IV Reactors

Within the last ten years, the Department of Energy and a group of representatives from Argentina, Brazil, Canada, France, Japan, Republic of Korea, South Africa, the United Kingdom, and the United States began to meet to develop the next generation of Nuclear energy systems. [1] No new nuclear reactor has come online in the US since Watts Bar 1 in 1996, [2] and until last September, no nuclear plant has been ordered for much longer. This new wave of nuclear energy plants, coined Generation IV (Gen IV) is intended to be economically competitive, safe, and efficient. [1] The six nuclear systems termed Gen IV are the Very-High-Temperature Reactor (VHTR), the Supercritical-Water-Cooled Reactor (SCWR), Gas-Cooled Fast Reactor (GFR), Lead-Cooled Fast Reactor (LFR), Sodium-Cooled Fast Reactor (SFR), and Molten Salt Reactor (MSR). [3] These reactors all operate at higher temperatures and some at higher power levels than the current light water reactors [3], and will need corresponding auxiliary and safety system improvements to keep up with the evolving nuclear plant designs.

One of the projects along with advancements in nuclear materials and new reactor core designs is the possibility of using nanofluids in these Gen IV reactors, as well as retrofitting current LWRs. Nanofluids are engineered fluids that contain a suspension of nanoparticles in a pure substance. A pure fluid is a substance that is uniform in chemical composition over its entire volume (such as water or ethanol). Nanofluids have shown to be promising as an alternative for a reactor coolant or as a safety system coolant to cover the core in the event of a loss of coolant accident. The promise of nanofluids stems from their superior heat transfer properties with respect to a pure substance. They have a slight enhancement compared to pure

fluids in conductive heat transfer [4], convective heat transfer [5], but most importantly, a great

enhancement (up to 200%) of critical heat flux (CHF). [6, 7]

CHF represents the upper limit for nucleate boiling, which in turns limits the performance

of reactor cooling systems. CHF is a transition that causes the wall temperature to jump by at

least several hundred degrees [8], typically followed by the heater failure. To keep a reactor core

from being damaged in the event of a power spike, the maximum power of a core must be kept

well below the value causing CHF on the surface of the fuel rods. The power peaking factor is

the parameter capturing the power non–uniformities that cause the development of hot spots in

the core. Obviously, the heat flux must be kept below CHF at the hot spot, and that will

automatically ensure that CHF is not reached anywhere in the core. For example, for a cylinder

(similar to the fuel used in current PWRs) with a reflector, the power peaking factor is 2.03, so to

avoid inducing CHF, the operational power must be half of the max power (excluding safety

factors). [9] This limitation reduces the overall cost-effectiveness and efficiency of liquid

cooled nuclear reactor systems. An improvement in CHF prevention can allow an increased

power density without an increased risk of a meltdown during a loss of cooling accident. [10]

1.2 Nanofluid Characteristics

The variety of nanoparticles used in the nanofluids covers a large range of metal oxides,

metals, and other materials including for example alumina, silica, gold, and diamond. These

nanoparticles are normally kept from agglomerating by one of two methods: pH control or with a

surfactant. [11] These nanoparticles have a diameter of 1-100 nm, [11, 12] and there is a log-

normal distribution of particle size.
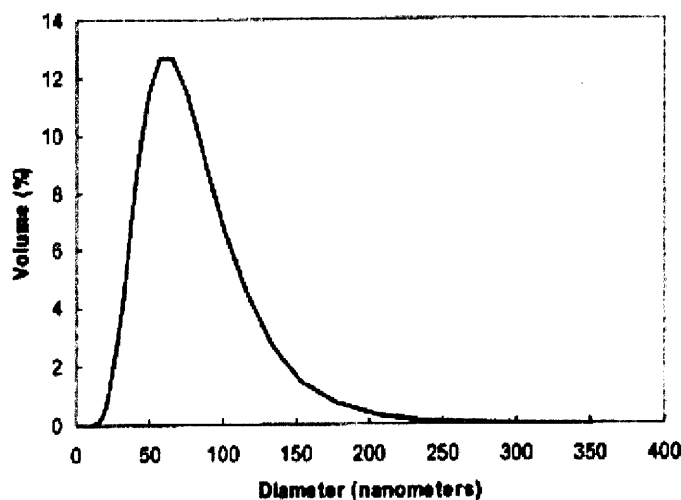
Figure 1-1: Distribution of Al₂O₃ nanoparticle sizes from Das et. al [4]

1.2.1 Nanofluids Application for PWR

As stated before, nanofluids have an enhancement over pure fluids with respect to

conductive and forced convection heat transfer. For conductive heat transfer there is an increase

in the thermal conductivity of nanofluids over the pure substance that is linear with volume

concentration of nanoparticles. [4, 11]
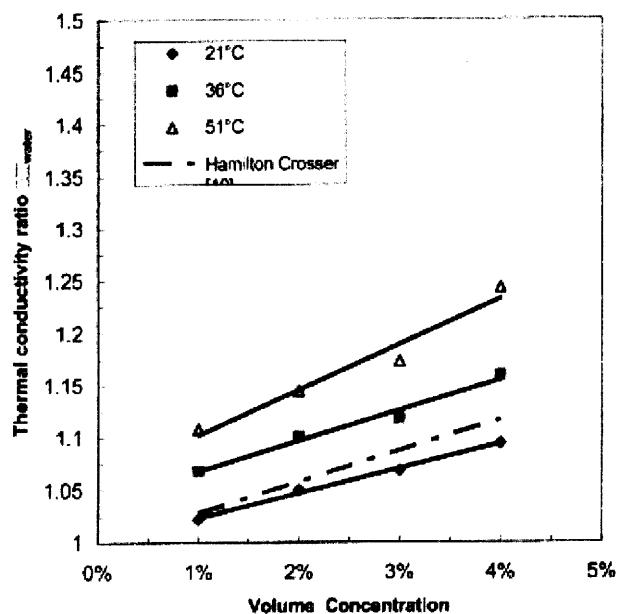
Figure 1-2: Thermal conductivity ratio vs. DI water at different temperatures and concentrations for Al₂O₃
[4]

Data from [4] shows that there is an increase in thermal conductivity. Alumina is not the

only nanofluid with an increase in conductivity. Shown in [11], there is an increase in

conductivity for ZnO in ethylene glycol and DI water.

More importantly, there is an increase in the convective heat transfer coefficient. In

nuclear reactors, the heat is removed from the fuel elements via forced convection, making this a

much more important heat transfer process. In both water and ethylene glycol, increasing

concentrations of alumina nanoparticles increases the heat transfer coefficient. [5]
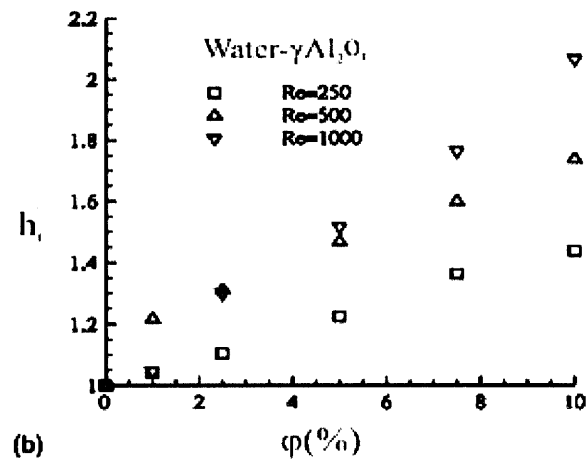
Figure 1-3: Heat transfer coefficient for alumina in DI water at different volume concentrations [5]

Although nanofluids exhibit better heat transfer properties than pure substances, they also

have a higher viscosity, which corresponds to an increase in pumping power. The ratio of

viscosities of a nanofluid to viscosity of a pure substance increases substantially as a function of

volume percent. [13]
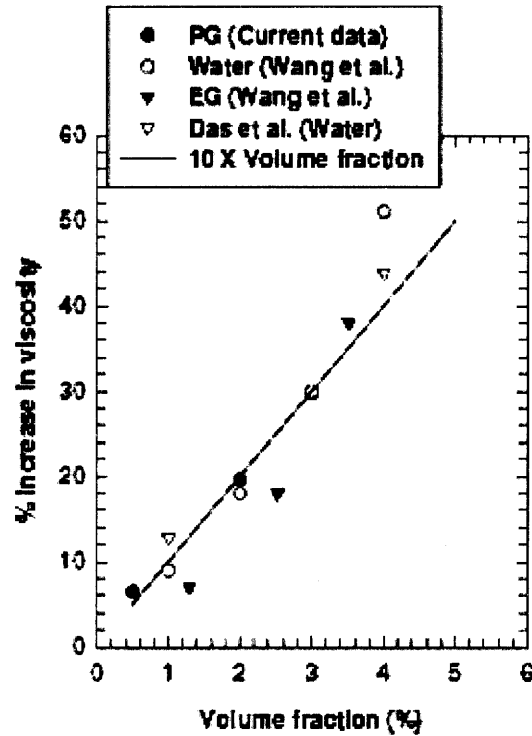
Figure 1-4: Percent increase in viscosity of Al₂O₃ nanofluids over water [13]

This increase in viscosity is accompanied by an increase in the necessary pumping power to provide flow through a reactor. For alumina nanofluid at a volume fraction of 5%, there is an increase is conductivity of about 10%, an increase in convective heat transfer of about 50%, and an increase in viscosity of about 50%. [4, 5, 13] The pumping power required for a closed loop is,

$$P_{Pump} = \Delta P \frac{m}{\rho} \qquad (1\text{-}1)$$

and the pressure loss (ΔP) is,

$$\Delta P = f \frac{l}{d} \frac{\rho v^2}{2} \qquad (1\text{-}2)$$

Following the procedure in [14], the pumping power for a turbulent flow of an incompressible fluid in a flow channel (pipe) is,

$$P_{Pump} = \frac{.092l}{d^{1.2} A_c^{1.8}} \left[\frac{\mu^{0.2}}{\rho^2} \right] \dot{m}^{2.8} \qquad (1\text{-}3)$$

and for laminar flow,

$$P_{Pump} = \frac{128l}{d^2 A_c} \left[\frac{\mu}{\rho^2} \right] \dot{m}^2 \qquad (1\text{-}4)$$

As the viscosity increases, the pumping power increases, depending on the type of flow. So as the heat transfer properties increase (with an increased concentration of nanoparticles), there will be a trade-off with the additional pumping costs.

The most remarkable property of nanofluids is the dramatic increase in CHF. All of these nanofluids have shown to increase CHF with a variety of heater shapes, surfaces, and composition. There are enhancements up to 200%. Vassallo et. al. [15] found an enhancement of 100% in .5% (volume) SiO_2 nanofluid, You et al.[7] showed 200% CHF enhancement in 0.005g/L Al_2O_3 nanofluids. Bang and Chang [16] observed enhancement in vertical and horizontal heaters in Al_2O_3 nanofluids. Additionally, Kim et. al. [17] found an enhancement in TiO_2 nanofluid at concentrations of 10^{-5} up to 10^{-1} (by volume).

The enhancement in CHF can potentially benefit existing plants, or for construction in new power plants to implement a power upgrade without reducing the safety margins. During the investigation of a 20% power increase compared to a Westinghouse PWR, a stated goal of nanofluids is to enhance CHF by 30% at less than .001% vol. [12] The low nanoparticle concentration is to ensure that the properties, especially viscosity, are the same as pure water. This power increase can be accommodated by an increased mass flow rate and/or an increase in core temperature rise. [12] Increasing power causes a reduction of the CHF margin which can be recovered by using a nanofluid.

2 CHF

CHF is the value of heat flux (power per unit area) at which boiling transitions from nucleate boiling to film boiling. This transition is undesirable in power systems, such as nuclear reactors, because once in film boiling, heat transfer is much less effective. This reduction in the heat transfer coefficient is followed by severe damage to reactor components so CHF must be avoided. The heat flux is related to the wall and bulk temperatures by Newton's law of cooling

$$q'' = h(T_w - T_b),$$ (2-1)

where h is the heat transfer coefficient, T_w is the wall or heater temperature, and T_b is the bulk fluid temperature, with the quantity $(T_w\text{-}T_b)$ known as the wall superheat. [8]

2.1 CHF Analysis

Although CHF is very important in heat transfer, there is no consensus on the exact physical mechanism. Over the years, many theories have been proposed, but none has gained a wider acceptance or proved to be much more correct than the others are. Most theories fall into one of the following categories. [6] These theories attempt to describe and predict CHF in pure fluids, but with the introduction of nanofluids, the following theories are unproven.

2.2 Hydrodynamic Instability Theory

First, the hydrodynamic instability theory states that the cause of CHF is due to the blockage of liquid to the heater surface by the rising vapor. [6, 18] As the liquid rushes down towards the heater, evaporation begins, which causes the newly created liquid-vapor interface to be pushed up. The vapor then escapes as a jet up through the liquid. The jets are not stationary and this system of boiling oscillates at a certain frequency. [18] This system of a dense fluid above a lighter fluid along with the two fluids of different densities flowing counter-directional gives rise to Taylor and Helmholtz instabilities. At low heat fluxes, only Taylor instabilities are

important, but near CHF, their combined effects are important because at CHF Helmholtz

instabilities cause the vapor streams to collapse. [18] By finding the propagation of instabilities

and solving for the vapor velocity,

$$u_v = \sqrt{\sigma V_m / \rho_v} \sqrt{\frac{\rho_l}{\rho_l + \rho_v}} \qquad (2\text{-}2)$$

where V_m, the wavenumber, is equal to $2\pi/R_{jet}$. Using the vapor velocity, the heat flux can be

calculated as,

$$q'' = C\dot{m}_v h_{fg} / A = C\rho_v u_v h_{fg} \qquad (2\text{-}3)$$

where C is a constant that Zuber calculated to be 0.131. So CHF is predicted by

$$q''_{CHF} = .131 h_{fg} \rho_v \left[\frac{\sigma g (\rho_l - \rho_v)}{\rho_v^2} \right]^{0.25} \sqrt{\frac{\rho_l}{\rho_l + \rho_v}} \qquad (2\text{-}4)$$

when eliminating the wave number. This equation predicts CHF solely on the fluid properties,

and given that nanofluids, especially at low concentrations, have almost identical properties to

their pure substance, this equation indicates that the CHF for nanofluids should be close to that

of the pure substance. As discussed earlier, CHF for Al_2O_3 in water at 10^{-5} by volume was found

to be higher by about 50%. [6] So this explanation is not sufficient to explain the CHF

enhancement in nanofluids.

2.3   Macrolayer Dryout Theory

Second, the macrolayer dryout theory, assumes that large bubbles, with long departure

times, are the trigger of CHF. The bubble is fed by many jets of vapor, and when the bubble

grows to an appropriate size, it departs. [6, 19] Beneath the large, mushroom shaped bubble,

there is a thin liquid layer, the macrolayer. As the heat flux increases, this theory postulates that

the number of vapor streams increases and the diameter of streams decreases, so that the overall

area of the vapor jets is constant. Finally, the ratio of the height of the jet to the diameter of the jet is constant so that as heat flux increases, the height decreases. [19]
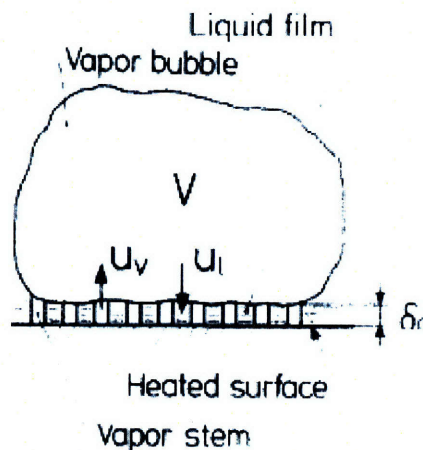
Figure 2-1: Diagram of the large bubble forming above a heater surface [19]

The figure above shows the vapor jets formed by bubbles that are forming the large vapor bubble, which will eventually depart. The macrolayer (δ) decreases with an increasing heat flux and at some point when the macrolayer dries out if the bubble has not yet departed, CHF occurs. The macrolayer can be estimated by using the contact angle of the fluid on the heater surface.
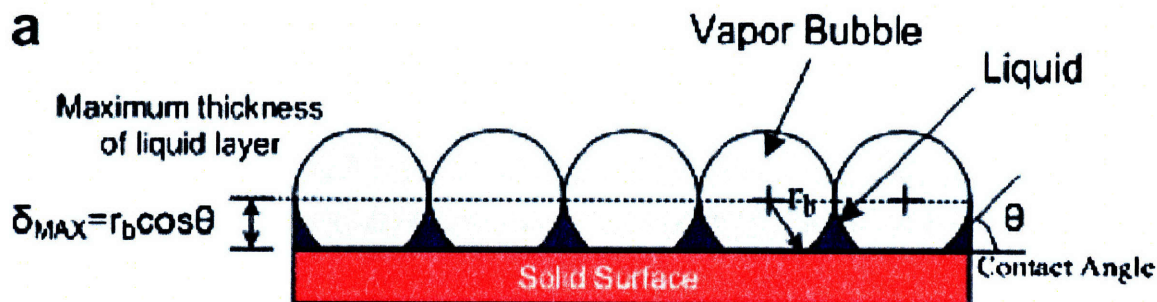
Figure 2-2: The macrolayer as shown by a series of bubbles and its relation to contact angle [6]

Figure 2-2 shows the development of the macrolayer beneath departing bubbles. As the contact angle increase, the maximum thickness of the macrolayer (dependent on $\cos\theta$) decreases. The equivalent macrolayer (averaged over the surface) can be described by,

$$\delta_e = r\,[\cos\theta - \frac{\pi}{12}(3\cos\theta - \cos^3\theta)] \qquad (2\text{-}5)$$

Additionally, the time that it takes the liquid layer to dryout is,

$$\tau_d = \frac{\delta_e \rho_f h_{fg}}{q''} \qquad (2\text{-}6)$$

and when the departure time of the bubble is greater than the dryout time, the macrolayer will

dryout. [6] When using the calculation for the macrolayer or a measurement of the macrolayer,

CHF can be predicted by, [20]

$$q_{CHF} = \rho_f h_{fg} \delta_e (1 - \alpha) f \qquad (2\text{-}7)$$

The macrolayer measurement must be made at a high heat flux (close to CHF) so that the CHF

estimate is more accurate. For a fluid with a lower contact angle, the macrolayer increases, and

this leads to a higher CHF. For example, a decrease in contact angle from 70° to 20° is a good

assumption for metal oxide nanofluids boiled surfaces. None of the nanofluids mentioned above

have shown such a great enhancement in CHF (fourfold), but this theory may be able to explain,

at least in part, the CHF enhancement due to surface deposition of nanoparticles. [6]

Table 2-1: Contact angle for various nanofluids on clean and boiled surfaces [21]

Fluid	Pure water	Al_2O_3 nanofluid			ZrO_2 nanofluid			SiO_2 nanofluid		
Nanoparticle concentration (%v)	0	0.001	0.01	0.1	0.001	0.01	0.1	0.001	0.01	0.1
Clean surface	79°	80°	73°	71°	80°	80°	79°	71°	80°	75°
Nanofluid boiled surface	8°–36° [a]	14°	23°	40°	43°	26°	30°	11°	15°	21°

This table shows that the estimate of the contact angle changing from 70° to 20° is not

unreasonable given time for the nanofluid to boil on the surface. None of the nanofluids

mentioned above have shown such a great enhancement in CHF (fourfold), but this theory may

be able to explain, at least in part, the CHF enhancement due to nanofluids.

Several studies have attempted to observe the macrolayer and correlate it to CHF. In [22,

23], a conductance probe is used to measure the thickness of the macrolayer. The water used in

these experiments had small amounts of potassium chloride added to increase the conductivity.

[23] Since water has a much higher conductance than vapor, a probe measuring the conductivity

from the heater surface to a distance above the surface can detect what the phase of the fluid

beneath it is. By rearranging and solving an expression for the macrolayer in [19], the

macrolayer thickness based on heat flux can be calculated as, [22]

$$\delta = .0107 \sigma \rho_v \left(\frac{\rho_v}{\rho_l}\right)^{0.4} \left(\frac{h_{fg}}{q''}\right)^2 \tag{2-8}$$

Many different pure fluids were tested experimentally in [22] and gave good agreement to the

theoretical model of macrolayer.
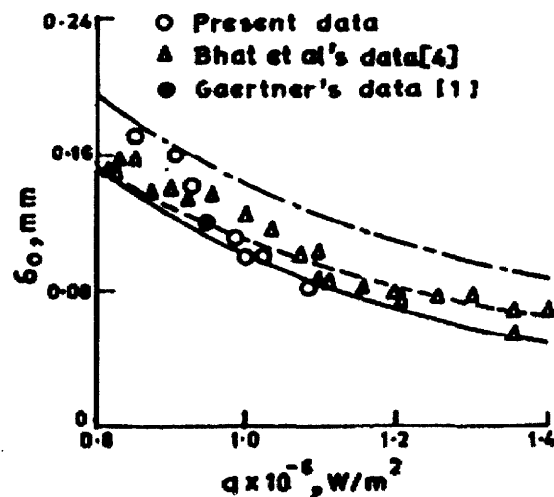
Figure 2-3: Experimental and theoretical data for macrolayer vs. heat flux in water [22]

When the fluid of interest is a nanofluid, equation (2-8) does not hold because although

the macrolayer is sensitive to contact angle, none of the other fluid parameters (the right side of

the equation) are sensitive. In [24], one of the theories about macrolayer formation is based on

the lateral coalescence of bubbles. This coalescence is further helped by the increase in

nucleation sites that corresponds with increased heat flux. [24] The radius of the forming

bubbles can be related to the area of the heater and more importantly the nucleation site density.

$$r = 0.5 \frac{1}{\sqrt{N_A}}$$

(2-9)

Additionally, the nucleation site density can be related to the heat flux by,

$$N_A = cq^2$$

(2-10)

where c is a constant that is dependent strongly on contact angle. [24] By combining equations

(2-5), (2-9), & (2-10) the macrolayer can be related to the heat flux, but including the wettability

(contact angle).

$$\delta_e = \frac{[\cos\theta - \frac{\pi}{12}(3\cos\theta - \cos^3\theta)]}{2q\sqrt{c}}$$

(2-11)
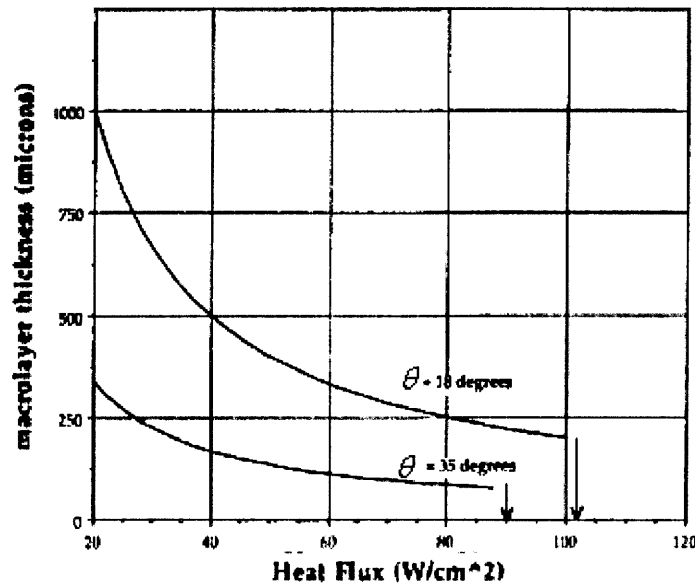
Figure 2-4: Macrolayer thickness vs. heat flux for different contact angles [24]

In another study, Buchholz et. al. used an optical probe to measure void fraction vs. probe

height in saturated isopropanol. Using an optical probe in different boiling regimes (onset of

nucleate boiling, nucleate boiling, and film boiling), these experiments provide a view of the

possible characteristics of the phase of the fluid close to a heater surface.
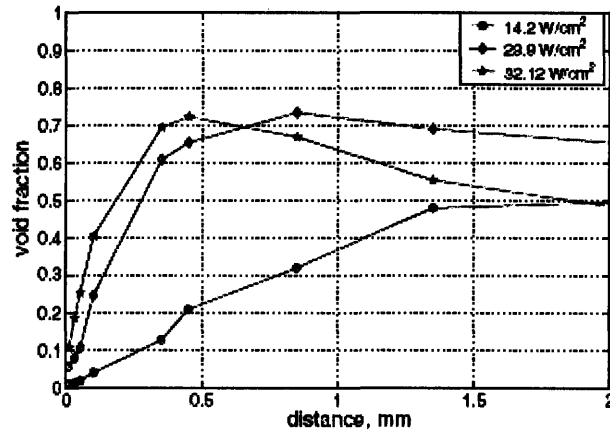
Figure 2-5: Void fraction vs. probe distance in isopropanol in nucleate boiling (low heat flux) [25]
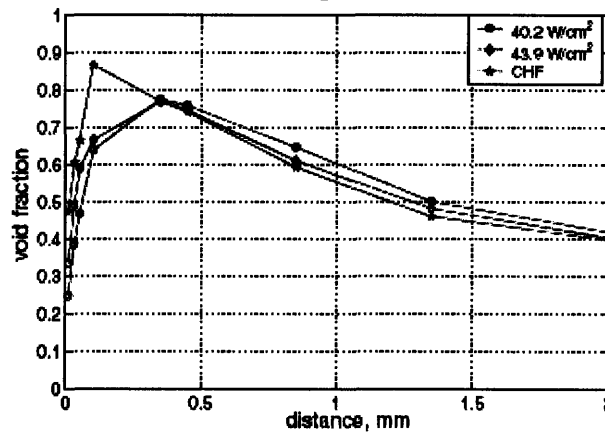
Figure 2-6: Void fraction vs. probe distance in isopropanol in nucleate boiling (high heat flux) [25]
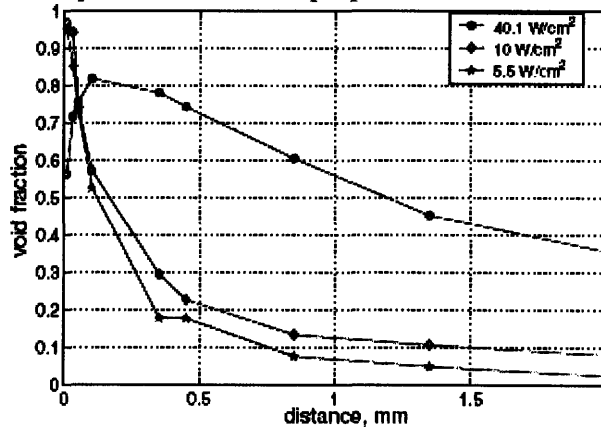
Figure 2-7: Void fraction vs. probe distance in isopropanol in film boiling [25]

These graphs indicate that with an increase in heat flux, the void fraction does increase, and more importantly the macrolayer thickness decreases, re-affirming results from [22] and agreeing with the theory from [19].

2.4 Hot/Dry Spot Theory

Third, the hot/dry spot theory, proposed by Theofanous and Dinh [26, 27] states that CHF is caused by hot/dry spots that do not rewet, which causes a temperature runaway on the surface. [6, 26, 27] As the heat flux goes above 200 kW/m^2, hot spots begin to appear. These are dry spots about 1 mm in diameter where the superheat of the heater goes up to 70°C (at high heat flux). [27] Reversible hot spots can be rewetted by the fluid rushing to the heater surface, but irreversible hot spots do not rewet and induce CHF. [6, 26]
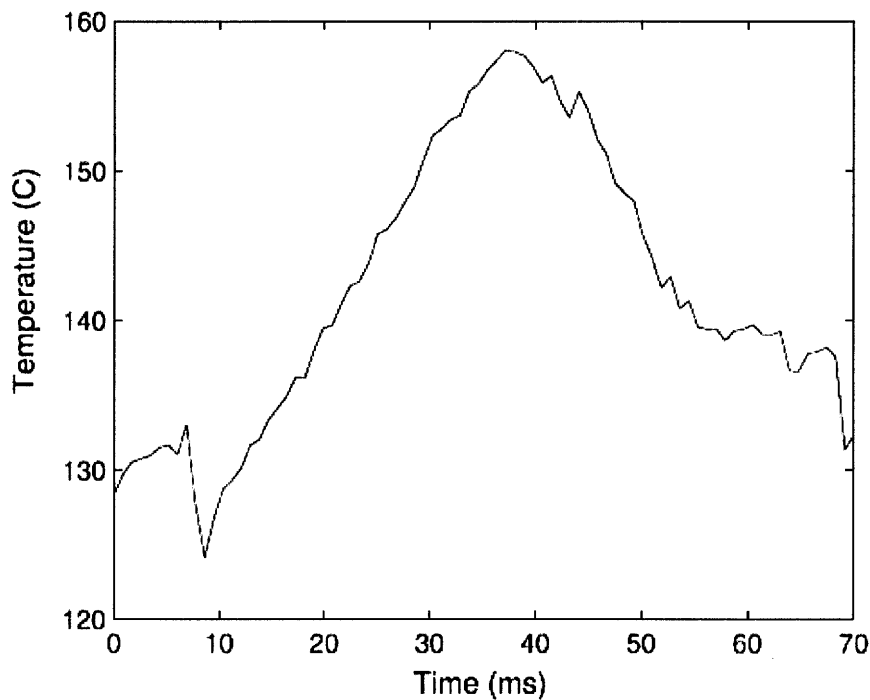
Figure 2-8: Time profile of temperature of a nucleation site that goes through reversible dryout [27]

Theofanous and Dinh state that the recoil force of the evaporation forces the liquid back, and when it reaches a certain value the liquid cannot push back to rewet the dry spot, inducing an irreversible hot spot and CHF. [6, 26, 27] Using this concept, they derived a new expression for CHF,

$$q_{CHF}^{"} = \frac{1}{\sqrt{\kappa}} \rho_g h_{fg} \left(\frac{\sigma g (\rho_f - \rho_g)}{\rho_g^2} \right)^{0.25} \qquad \text{(2-12)}$$

which is very similar to the Zuber correlation except for the factor κ, which is dependent on the wettability of the surface. Although Theofanous and Dinh do not provide an explicit correlation for κ, it can be estimated according to [6] as,

$$\kappa = \left(1 - \frac{\sin\theta}{2} - \frac{\pi/2 - \theta}{2\cos\theta} \right)^{-0.5} \qquad \text{(2-13)}$$

So for a well wetting surface, κ will be smaller than for a poorly wetting surface.

It is possible that nanoparticles contribute to a higher CHF in this model by increasing conduction on the surface of the heater and the fact that an increased wettability induces rewetting of the heater surface. [6] This model possibly can explain the CHF enhancement as well.

2.5 Bubble Interaction Theory

Fourth, the bubble interaction theory states that the increased number of bubbles departing from the surface at high heat flux will coalesce and prevent rewetting of the surface. [6, 28] According to [28], the heat flux can be described as,

$$q" = C_q h_{fg} \rho_v N \pi / 6 * D^3 f \qquad \text{(2-14)}$$

where C_q is a factor that depends on the geometry of the bubbles forming. If the bubbles are forming and touching, $C_q = 1$, but reduces when CHF occurs. [28] This implies that the heat transfer reduces when the superheat is raised above a certain point, which does occur in transition boiling.

3 Optical Probe Operation, Experiment Setup, and Results

3.1   Optical probe operation

In order to investigate the Macrolayer Dryout Theory, an optical probe will be used to

determine the phase (gas or liquid) of the fluid that it is in contact with. According to Snell's

law, a beam of light passing through one medium to another is refracted according to:

$$\frac{\sin \theta_1}{\sin \theta_2} = \frac{n_2}{n_1}$$ (3-1)

where n_1 and n_2 are the refractive indices of the medium. In the case of an optical probe emitting

a beam of infra-red light from a fiber-optic cable to either water or air, for a given angle ($\theta_{c,water}$

$\geq \theta \geq \theta_{c,air}$), the beam will be refracted in water, but reflected in air. [29] The optical probe is

built upon this principle so that there is a different signal depending on the phase at the tip.
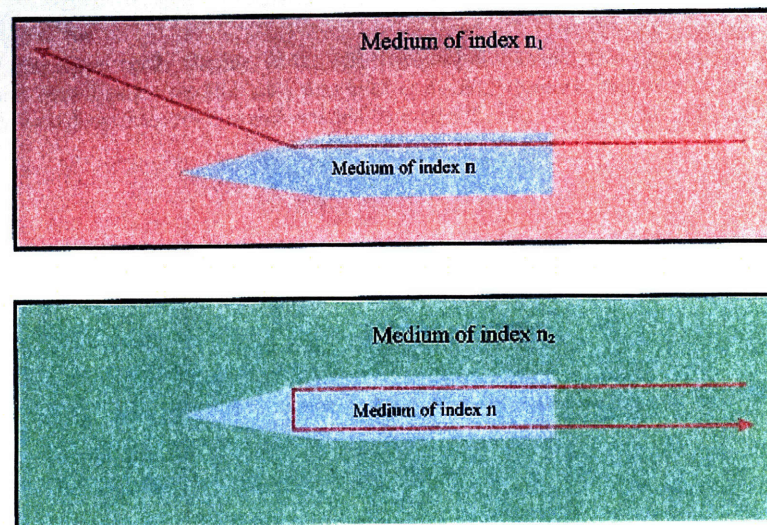
Figure 3-1: Optical probe beam in water (top) and air (bottom) [30]

The returning signal (or lack thereof) gives an indication of phase, which is recorded and

analyzed by the software in a variety of methods. [31] The probe returns a voltage value (0 or 5

V) depending on the phase (5V indicates gas, 0V indicates liquid). The optical probe directly

measures number of bubbles, flight time of bubbles, and the vapor time. [31] However, it does

not directly measure diameter or velocity of the bubbles. Software is used to derive the values of

diameter and velocity by time correlating the vapor time raw data via an algorithm that makes

some assumptions on bubble shape and statistical distribution. These values can be viewed in a variety of ways on the Interface for Optical Probe (ISO) software.

3.2   Optical probe validation

To ensure that the probe is functioning properly, it was validated for several fluids using bubbles created from an air hose. The values provided by the probe are validated by comparing them to direct camera observations and bubble theory, as discussed below. To find the expected bubble diameter, the surface tension is balanced with the buoyancy force to find the expected diameter

$$d_b = \sqrt[3]{\frac{6\sigma D_{inj}}{g(\rho_l - \rho_g)}} \qquad (3\text{-}2)$$

where σ is the surface tension, ρ is the density, and D_{inj} is the diameter of the air injector. To better control this validation, it was performed at room temperature, so to create bubbles, an air injector was used. To find the expected bubble velocity, three dimensionless numbers are used to determine the shape of the bubbles; the Morton, Eotvos, and Reynolds numbers,

$$Mo = \frac{g\mu_l^4}{\rho_l \sigma^3} \qquad (3\text{-}3)$$

$$Eo = \frac{(\rho_l - \rho_g)g d_b^2}{\sigma} \qquad (3\text{-}4)$$

$$Re = \frac{\rho v d_b}{\mu} \qquad (3\text{-}5)$$

where ρ is the density of the fluid, σ is the surface tension, μ is the viscosity, v is the bubble velocity, and d is the bubble diameter. For non-spherical bubbles, the value used for d was the equivalent diameter. This value of equivalent diameter is the diameter that an irregular bubble would have with the same volume as a bubble with an equal volume. The value in this case for elliptical bubbles ended up being $2\sqrt[3]{ab^2}$, where a is the minor axis, and b is the major axis of the ellipse. The velocity can be found either through analytical correlations if the bubble are

spherical or spherical cap regime, or using the figure below, in conjunction with the values of

Mo, Eo, and Re in the more general case.
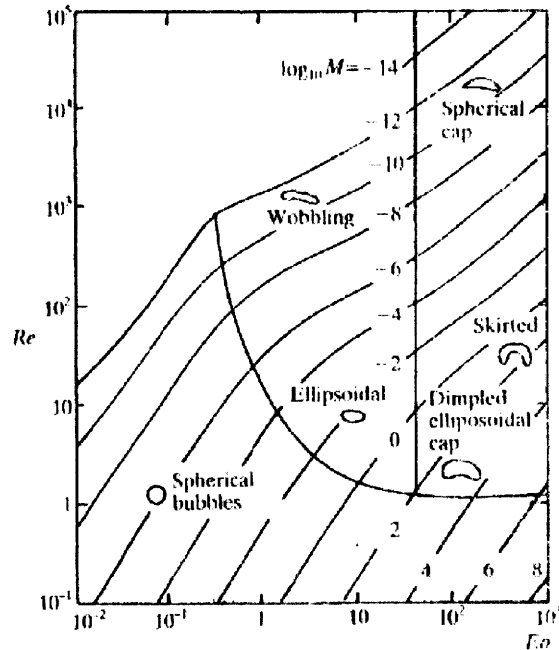
Figure 3-2: Correlation of Re (y-axis) vs. Mo (diagonal lines) and Eo (x-axis) [32]

The outputs of the calculations are average bubble diameter, velocity, void fraction, and

departure frequency. Before use, however, the optical probe's measurements must be verified.

3.3   OP Setup and Procedure

The probe only measures number of bubbles, flight time of bubbles, and the vapor time

[31], and it is assumed that these data are correct with negligible uncertainty. Using these data

and taking into account that the two probe tips are 1mm apart, other values such as diameter,

velocity, departure frequency, etc., can be derived from the raw data.
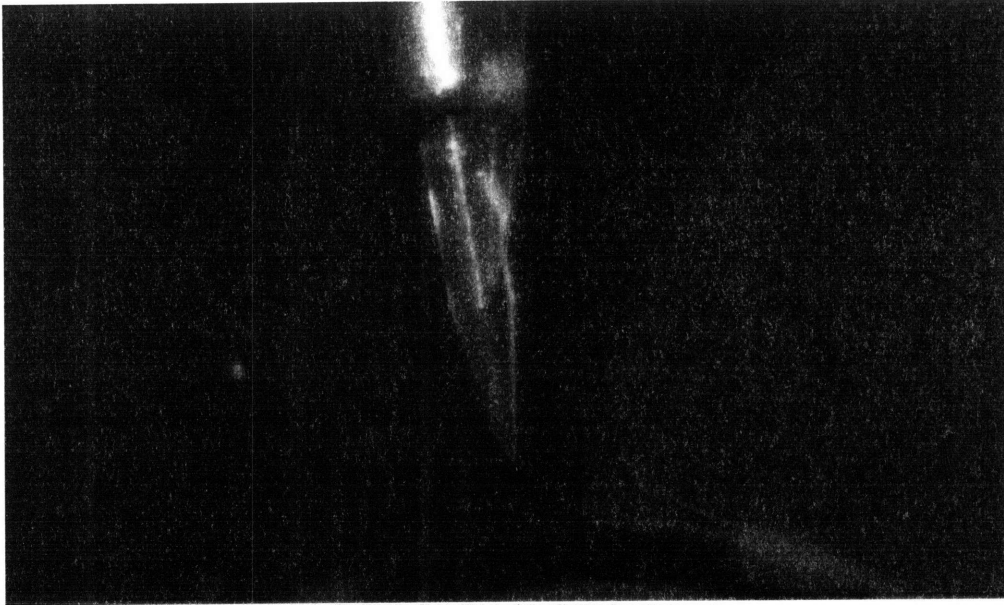
Figure 3-3 : Optical probe tips

Because the values for diameter and velocity are derived, they have the potential for being incorrect due to data processing errors. To simulate boiling without introducing too many bubbles that may confuse the software, an air-water setup was used where bubbles were made using air that was injected into the fluid.

This setup allowed for strict control of bubbles in order to independently measure them for comparison to the probe calculations and the theoretical values. The independent measurement is done by using a camera. While bubbles are in flight, a picture is taken with a very fast shutter speed (>1/250s).
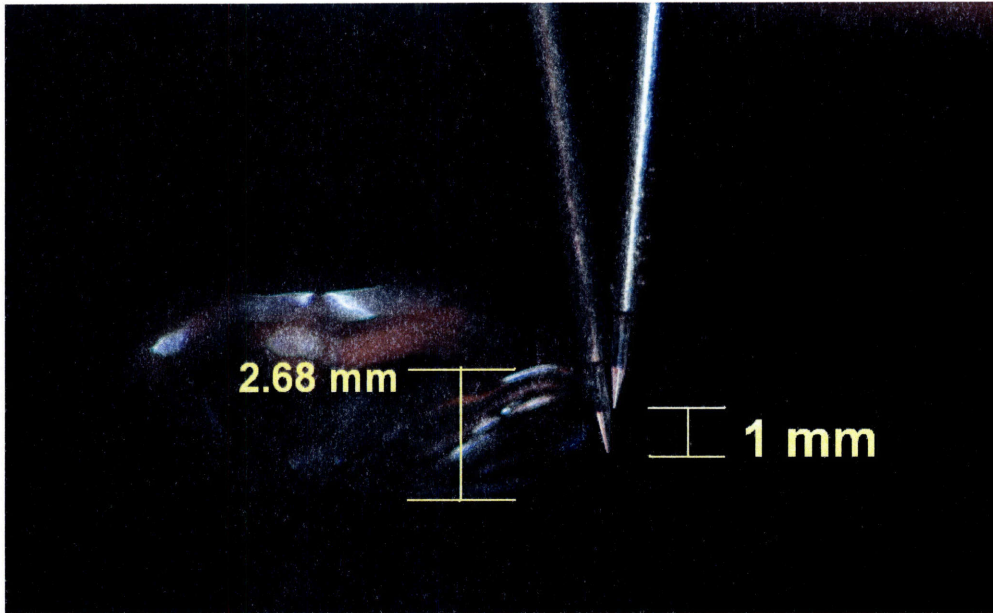
Figure 3-4: Sample picture of diameter validation with the probe tips used as the scale (1mm)

Since the shutter speed is so fast, the bubble moves very little and a measurement can be taken of

the bubble size in pixels. Next, another picture is taken at a low shutter speed, (~1/30s) to

measure the velocity.
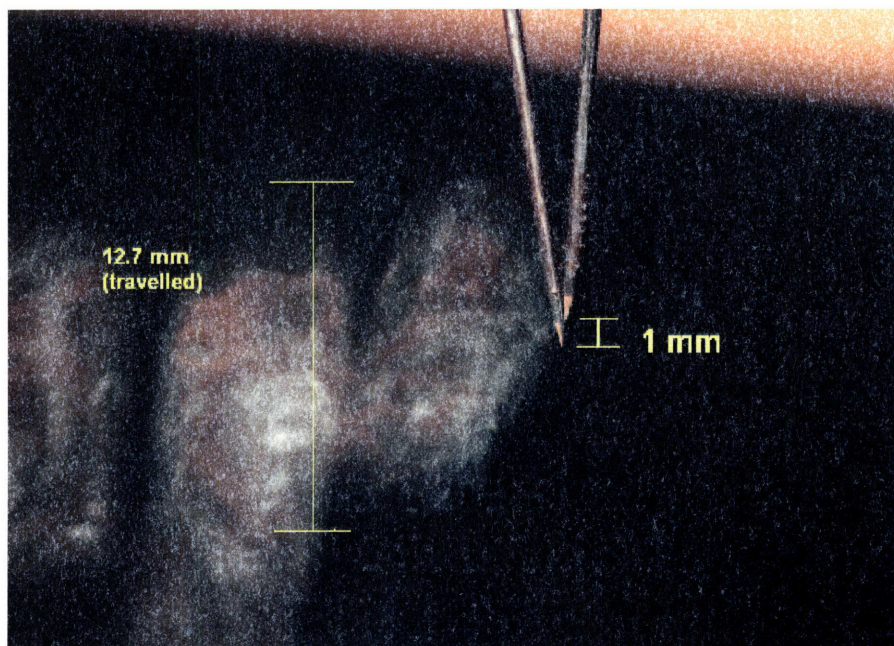
Figure 3-5: Sample picture for velocity validation

For every bubble in this picture, there is a streak due to the slow shutter speed. Just like the

diameter measurement, the length of the streak can be measured in pixels. Another picture is

taken to establish a scale for the number of pixels per mm. From here, the diameter is found using the scale and the velocity is found by subtracting the diameter (in pixels) from the streak and dividing by the shutter speed.

To house the bubble generator, a large, clear tank is needed to allow the bubbles to develop as well as be able to take pictures from a close distance to ensure good resolution for measurement. In addition, a threaded hole is placed on the top lid to allow the probe to be inserted into the tank.
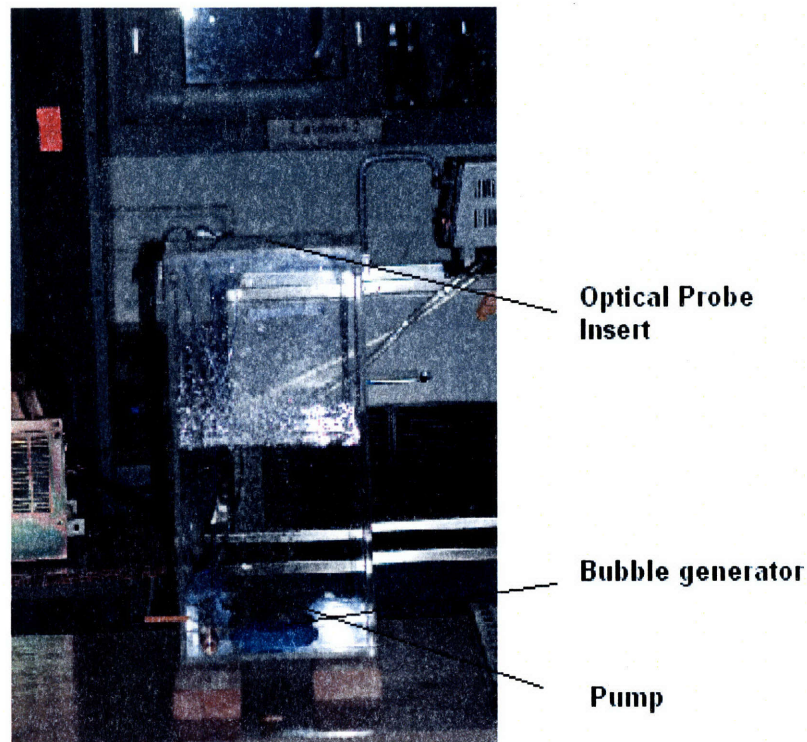
Figure 3-6: Experimental setup with bubble generator

3.4   OP validation results

Before obtaining results, it was clear that the size and shape of the bubbles in water was not spherical. This presents a problem to the optical probe because it can only measure dimensions in the vertical direction. A bubble that is spherical with diameter d will appear to be the same size as an elliptical bubble with minor axis of length d. By calculating the Mo and Eo numbers, the bubble regime (spherical, wobbling, elliptical, spherical caps, etc.) can be

determined, which should indicate how much accurate the probe software should be when assuming that the bubbles are spherical. Shown below are the expected bubble properties for various fluids and their expected regimes.

Table 3-1: Fluid properties, expected values for diameter, velocity, Mo, Eo, Re, and bubble shape [33-36]

Fluid name	σ (N/m)	ρ (kg/m^3)	μ (Pa*s)	Expected Diameter (mm)	Mo	Eo	Re	Expected Velocity (m/s)	Regime
Carbon tetrachloride	0.0270	1584	0.000901	1.577	2.071E-10	1.4302	700	0.2525	Wobbling
Mercury	0.4360	13500	0.001526	1.952	4.75E-14	1.1558	6000	0.3475	N/A
Water	0.0727	1000	0.001	2.558	2.55E-11	0.8819	500	0.1955	Wobbling
Ethanol	0.0228	789	0.0012	1.881	2.173E-09	1.1994	100	0.0809	Wobbling/ Spherical
Acetone	0.0253	784	0.00032	1.951	8.094E-12	1.1561	3000	0.6276	Wobbling
glycerin	0.0634	1261	1.5	2.114	154.38612	0.8713	0.1	0.0563	spherical
ethylene glycol	0.0477	1113	0.021	2.005	1.578E-05	0.9189	10	0.0941	Border

The expected diameter of all the fluids, except for R-123 was calculated by balancing the surface forces with the buoyant forces. The expected diameter of R-123 was calculated with an equivalent diameter $D_{eq}=D_b/\sqrt{2}$. Where D_b was the diameter calculated from eq. (3-2). The Re number was determined from Figure 3-2 and the velocity was calculated from the Reynolds number.

Water is a clear choice for testing the probe because even though the bubbles may not be spherical, many of the nanofluids to be tested are water based, so the probe must be accurate in water. Glycerin seems to be the most promising fluid because it is in the spherical regime under atmospheric conditions, so should provide a good bubble shape to test the probe. Ethanol and ethylene glycol appear to be other promising fluids because they are on the border of the wobbling and spherical regimes.

Table 3-2: Diameter and velocity validations for all water trials

Trial	Flow rate (ft³/hr)	Probe Diameter (mm)	Probe Velocity (m/s)	Validation Diameter (mm)	Validation Velocity (m/s)		Percent Error Diameter (%)	Percent Error Velocity (%)
2/9 Water	0.1	3.185	0.3425	4.31	0.3414		26.10209	0.322203
2/9 Water	0.2	3.885	0.395	4.503	0.38068		13.72418	3.76169
3/7 Water	0.1	3.04	0.402	3.68	0.413		17.3913	2.663438
3/7 Water	0.2	3	0.415	3.83	0.457		21.67102	9.190372
3/7 Water	0.3	3.88	0.43	4.52	0.469		14.15929	8.315565
3/7 Water	0.4	3.98	0.435	4.77	0.542		16.56184	19.7417
3/7 Water	0.6	4.42	0.447	4.52	0.513		2.212389	12.8655
3/7 Water	0.8	4.81	0.447	4.88	0.545		1.434426	17.98165
3/21 Water	0.1	2.2285	0.345	3.103	0.374		28.1824	7.754011
3/21 Water	0.2	2.555	0.3975	2.81	0.402		9.074733	1.119403
3/21 Water	0.3	2.81	0.4025	3.19	0.416		11.91223	3.245192
3/21 Water	0.4	2.95	0.4225	3.52	0.458		16.19318	7.751092
4-4 Water	0.1	2.1525	0.375	2.56	0.323		15.91797	16.09907
4-4 Water	0.15	2.1825	0.3825	2.77	0.337		21.20939	13.50148
4-4 Water	0.2	2.6175	0.39	3.2	0.418		18.20313	6.698565
4-4 Water	0.25	2.8625	0.3875	3.42	0.426		16.30117	9.037559
4-4 Water	0.3	3.1675	0.4075	3.59	0.438		11.7688	6.96347
4-4 Water	0.4	3.1825	0.41	3.86	0.452		17.55181	9.292035
						Average	17.89572	8.86051
						Std. Dev.	11.93432	5.17712

The trials for water proved successful, where the probe could calculate the diameter and velocity with a standard deviation of 11.9% and 5.1% respectively despite the wobbling bubbles. Of the remaining fluids to be tested, glycerin, ethylene glycol, and ethanol all were not nearly as accurate as the water was.

In the case of glycerin and ethylene glycol, the bubbles were not registered by the probe. They merely bounced off the tips due to the high viscosity of the fluid.
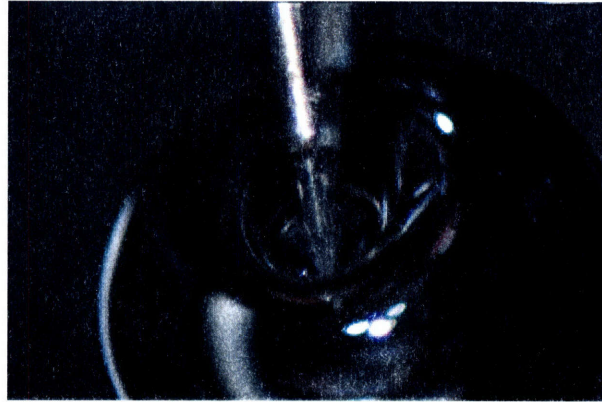
Figure 3-7: Air bubble in glycerin deforming around the probe tip

For ethanol, the small diameter size although promising in forming spherical bubbles, was problematic because a large number of bubbles were produced for a given amount of air. At times these bubbles very nearly coalesced into a jet. Although they were separate bubbles, the probe could not detect them individually and returned a signal of 100% (or close to it) void fraction during the test. In addition, camera validation was nearly impossible because the bubbles were so close together it was hard to distinguish them apart. Below are some of the graphs of diameter and velocity validation. They include the error bars of the probe measurement, which is calculated above. The camera validation error bars are also present, but due to the very good resolution of the camera, the error bars are on the order of microns (1/1000 of a mm).
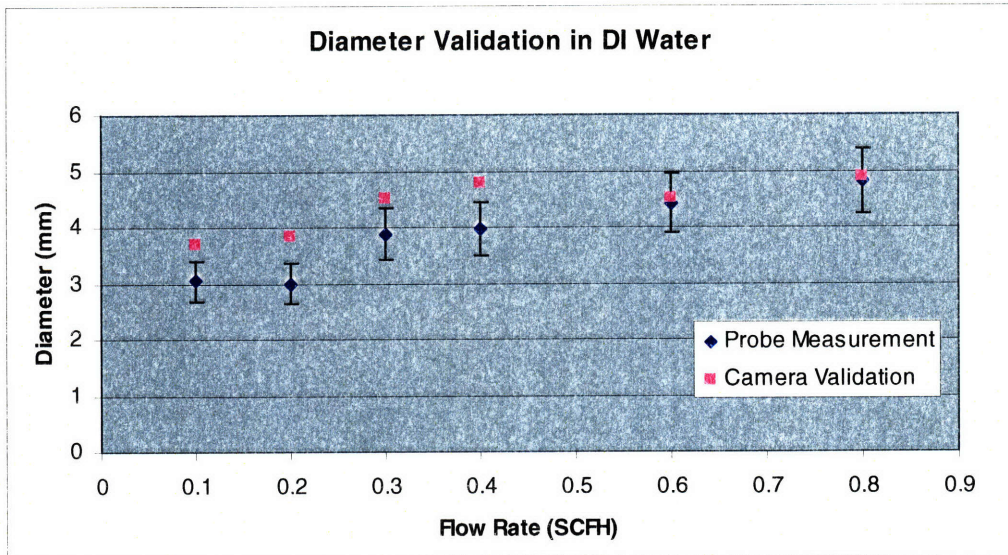
Figure 3-8: Diameter validation for one of the DI water trials
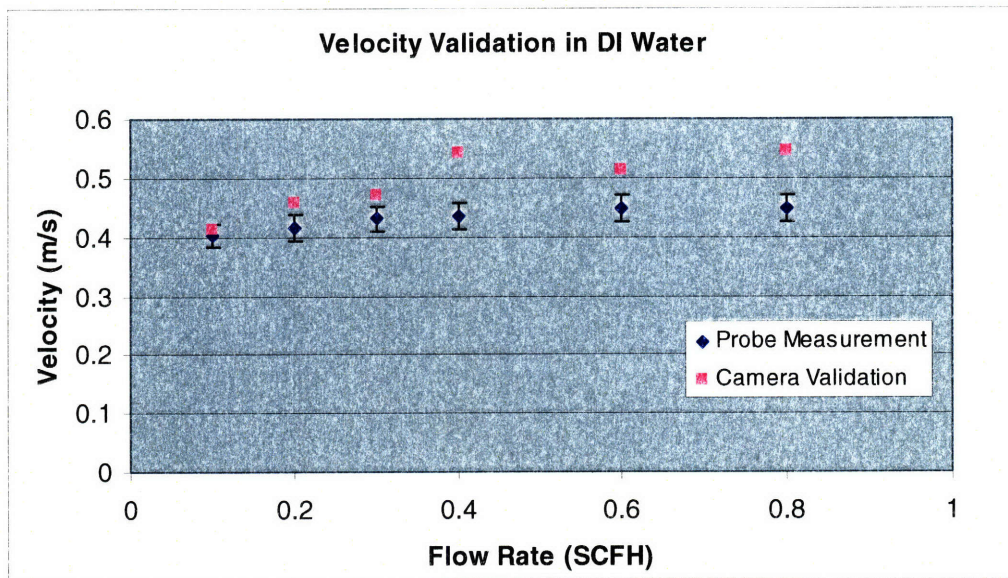

Figure 3-9: Velocity validation for one of the DI water trials

Another fluid, R-123 was used, and again the probe returned similar results as water,

calculating the diameter and velocity with a standard deviation of 10.3% and 7.1% respectively.
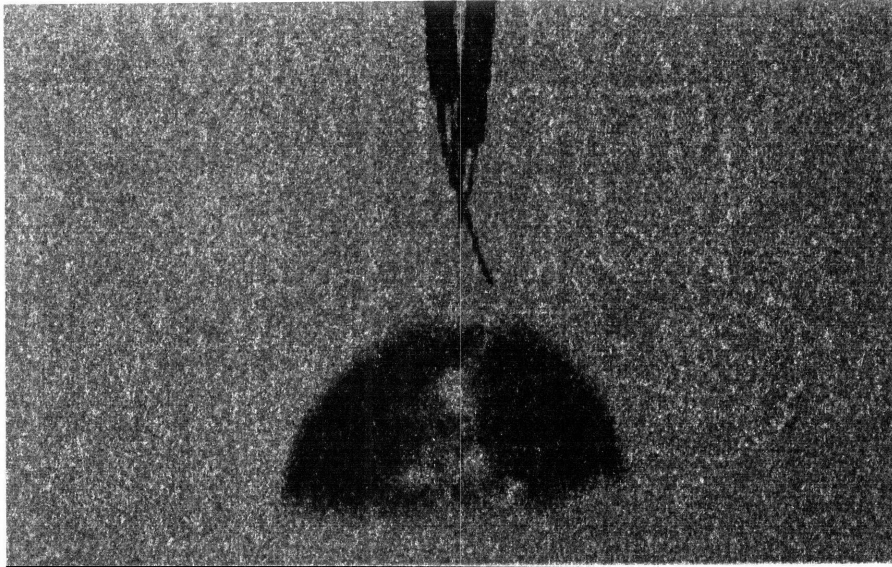
Figure 3-10: Spherical cap type bubble produced from air injection in R-123

Table 3-3: Diameter and Velocity Validation for R-123 Trials

Flow	D_Theory (mm)	Probe Diameter (mm)	Camera Diameter (mm)	% Error	V_Theory (m/s)	Probe Velocity (m/s)	Camera Velocity (m/s)	% Error
0.01	1.3800	1.9450	2.5700	24.3191	0.1167	0.1575	0.1417	11.1503
0.025	2.3400	4.8800	3.6000	35.5556	0.1523	0.2125	0.2245	5.3452
0.05	3.0100	5.3200	4.4100	20.6349	0.1720	0.2333	0.2174	7.3137
0.1	3.8131	4.8775	5.0912	4.1979	0.1941	0.2300	0.2332	1.3629
0.125	4.7927	5.7750	4.9783	16.0025	0.2176	0.3250	0.2691	20.7908
0.15	4.3196	4.7150	5.6337	16.3069	0.2066	0.2900	0.2820	2.8543
			Avg. % Error	19.5028			Avg. % Error	8.1362
			Std. Dev. (%)	10.3815			Std. Dev. (%)	7.0918

Similar to the validation above, the graphs of the R-123 validation are shown below with their

corresponding error bars.

Diameter Validation for R-123
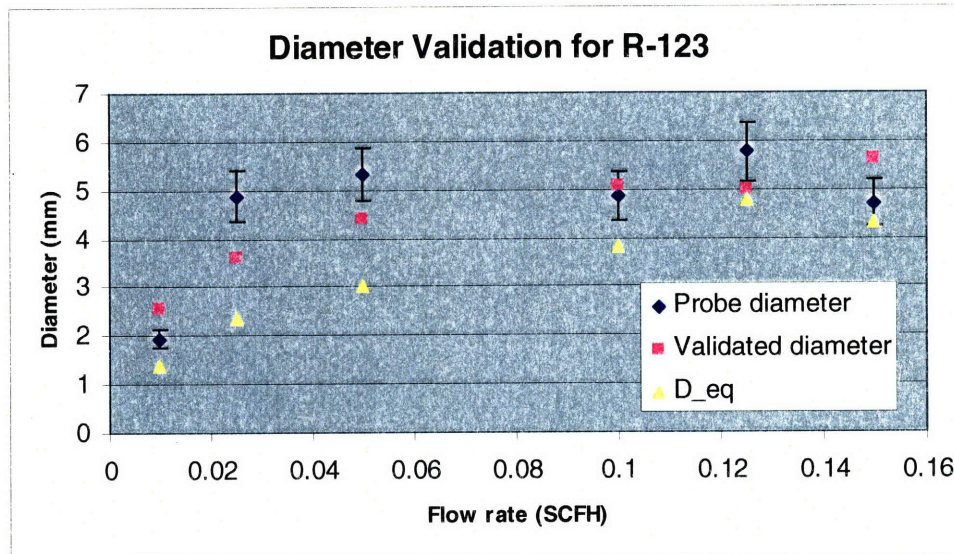
Figure 3-11: Diameter validation for one of the R-123 water trials

Velocity Validation for R-123
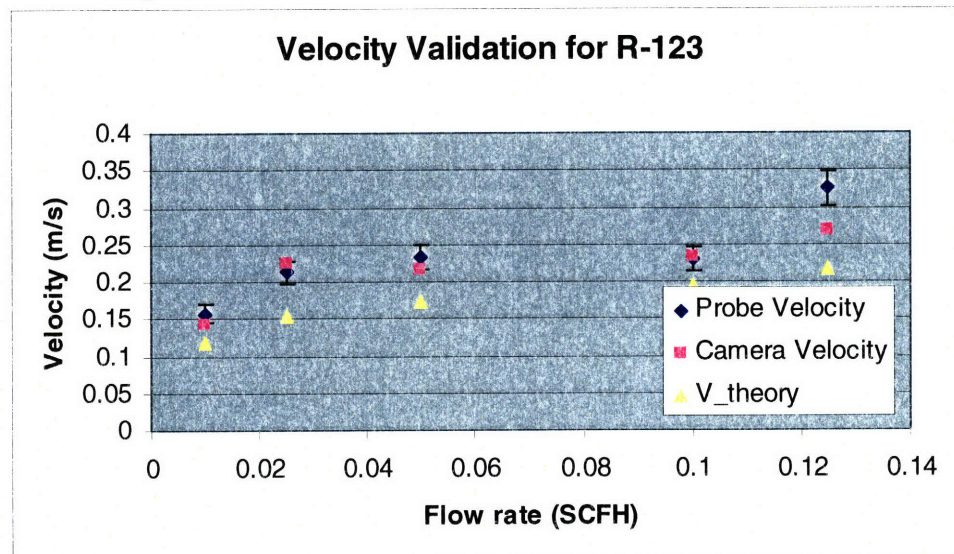
Figure 3-12: Velocity validation for one of the R-123 water trials

4 Pool Boiling Experiment (PBE) Setup and Results

4.1 Pool Boiling Experiment (PBE) Setup

The most important challenges of designing a facility are calibrating the distance of the probe tip to the heater and ensuring that only the heater dissipates power (vs the electrodes), and only dissipates power through its upper surface. The method used in [25] to measure the

distance of the probe from the surface consisted of using a stainless steel wire to pass a small

current between the heater (with current flowing) to a detector.
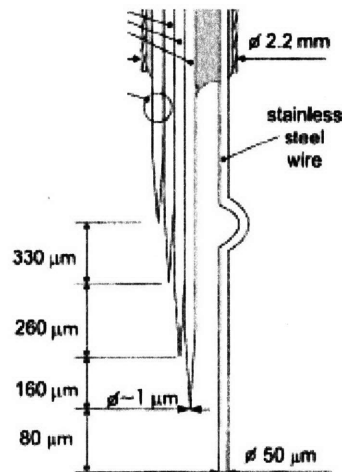
Figure 4-1: The probe tips from [25], with a wire attached to determine a reference distance

For good electrical contact between the wire (shown above with d=50μm) and the heater, the

heater must be made of some metal, preferably stainless steel. This setup is adopted to determine

a reference distance in this experiment.

The other challenge was to dissipate power on the heater surface, and nowhere else. The

steel has a relatively low resistivity; this means that to provide enough power to reach CHF, the

current must be high. A high current through the electrodes can result in significant Joule

heating in the electrodes, so their resistance should be decreased. Copper is used because of its

low resistivity (ρ_{SS}/ρ_{CU}~1/50), and furthermore, the electrodes cross sectional area is increased to

further lower the resistance.
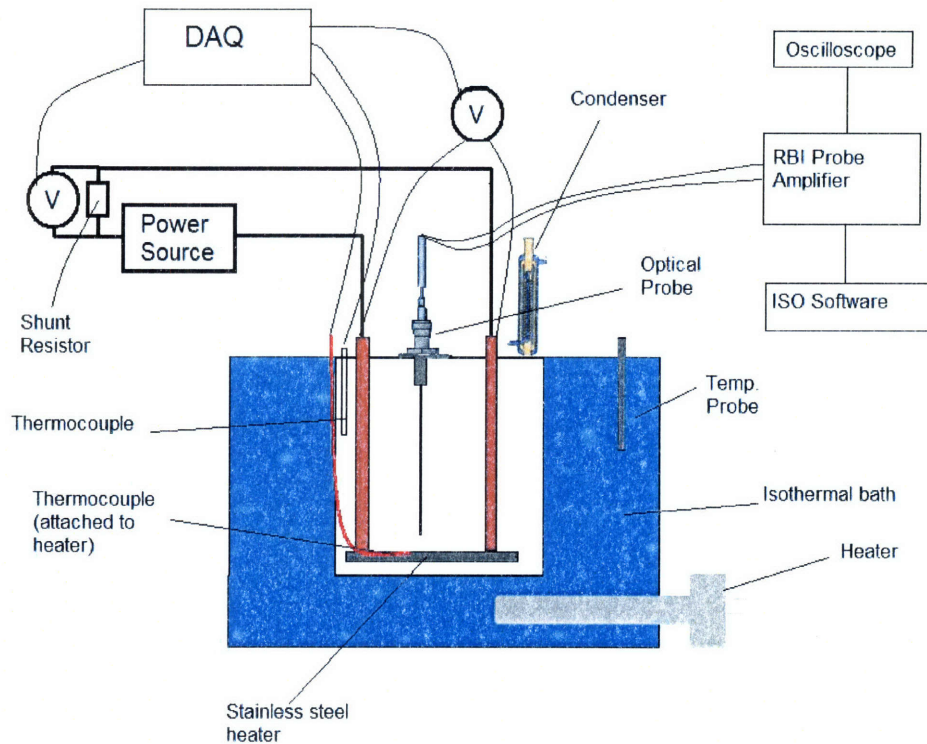
Figure 4-2: Experimental setup for the PBE facility
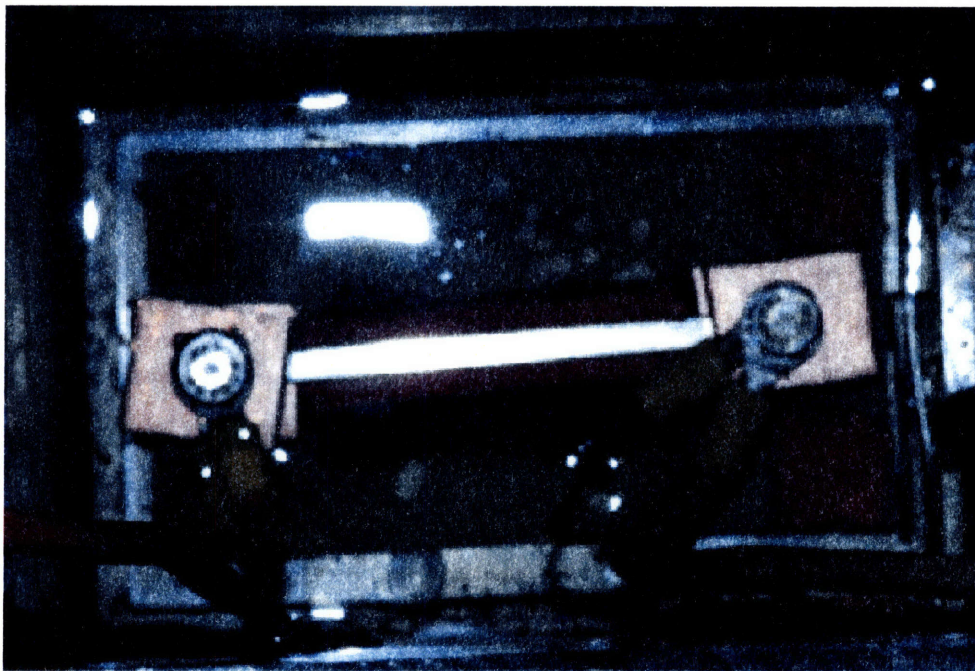
Figure 4-3 : Heater design

The heater is cut from a stainless steel sheet that has been sandblasted, cut using a water jet, then

sandblasted again. Sandblasting is done to create a high-heat-transfer surface that can ensure the

repeatability of the CHF tests. A thermocouple is spot welded to the bottom, the heaters are then insulated with silicone on the bottom side to prevent boiling from that side.

A condenser is also added to the top of the rig to reduce vapor escape into the lab environment. Also, the nanofluids are diluted to specific concentrations, so if there is evaporation, the nanoparticle concentration will increase as the liquid mass decreases. Surrounding this test facility is an isothermal bath of water to keep the inner bath at saturation temperature ($T_{bath}=100°C$).

4.2   Procedure

To do the macrolayer measurements, a stainless steel, sandblasted heater of area .00035 m^2 is used. The power supply is set to current control and is stepped up in increments to the desired heat flux where the power is held steady and the required optical probe measurements are taken. The heat flux is calculated as

$$q'' = \frac{IV}{l_h w_h}$$
(4-1)

where $l_h w_h$ is the area of the heater. The current is measured by a shunt connected in series with the power supply and the voltage is measured by measuring the voltage difference at the base of the electrodes as seen in fig. 4-7. These two signals are then fed into a data acquisition system (DAQ) where the power and heat flux can be calculated. To measure the temperature of the heater and the surrounding baths, several K-type thermocouples are used. There is one thermocouple in the outer bath, one in the inner bath, and one attached to the bottom of the heater. Only the last two are fed into the DAQ and recorded. These two signals are converted into a temperature then are used to measure the superheat (T_h-T_b). The comparison of heat flux vs. the superheat can be used to create a boiling curve.

At several heat fluxes (about 200 kW/m^2 apart), the optical probe is used to make probe height vs. void fraction measurements. Before making measurements, a reference distance must be established. The distance from the tip of the wire to the probe is measured using a Nikon D200 camera. The resolution allows the measurement to be accurate up to 5 µm. With this reference distance established, the probe is lowered until there is electrical contact (resistance drops greatly) with the reference wire. At that point, the height is known and the probe can be lowered. Once at a stable power and heater temperature, the probe is lowered to its minimum distance (~30µm) and after recording for up to 30 seconds with the ISO software, the probe is moved to a higher distance up to 1 mm above the heater surface.

Since the probe uses fiber-optic cables to transmit light to the tip and back, when the probe is close enough to the heater, the light may be reflected back to the cable. Even if there is liquid (light refracts), if the probe is too close to the surface, the signal may be returned, which indicates a gas phase. In [25], the signal ramps up beginning around 8 µm, which is the size of

the active area of the probe tip. [25] The optical probe that will be used in this experiment has

an active diameter of 50 μm. This large active area may result in a signal that increases to the

point where it is not accurate below 50 μm. [37] This is reflected in the procedure by not going

below 50 μm, but this does not impact the experiment very much because the expected minimum

values of the macrolayer thickness are around 100 μm. [23]

4.3   PBE Results

The probe once verified was used to measure void fraction close to the surface. Using

the constructed PBE, several tests were performed to see if the results in [22, 23, 25] could be

produced. The macrolayer is defined here as the point where the curve deviates from its initial

steep slope (below 100 μm) rather than the point where there is a maximum heat flux. This point

where the slope changes rapidly seems to be a better indicator of the edge of the liquid layer

(void fraction ~0%) and the regions populated with bubbles (void fraction > 50%).

As seen in section 2.3, experiments have been performed that have tested the theoretical

change of macrolayer with heat flux. Before any formal experiments began, the operation of the

probe was tested to determine if the results in [25] could be reproduced. Shown below, figure 4-

4 shows a similarity between figure 2.5 (high heat flux) and 2.6 (film boiling). Although this is

for a different fluid (ethanol), the macrolayer thickness is on the correct order of magnitude, as is

the magnitude of the void fraction. The probe does have the capabilities to reproduce the results

of previous experiments, and it is clear that the large active area does not affect the more

important distances of measurement (~100-200 μm from the surface).
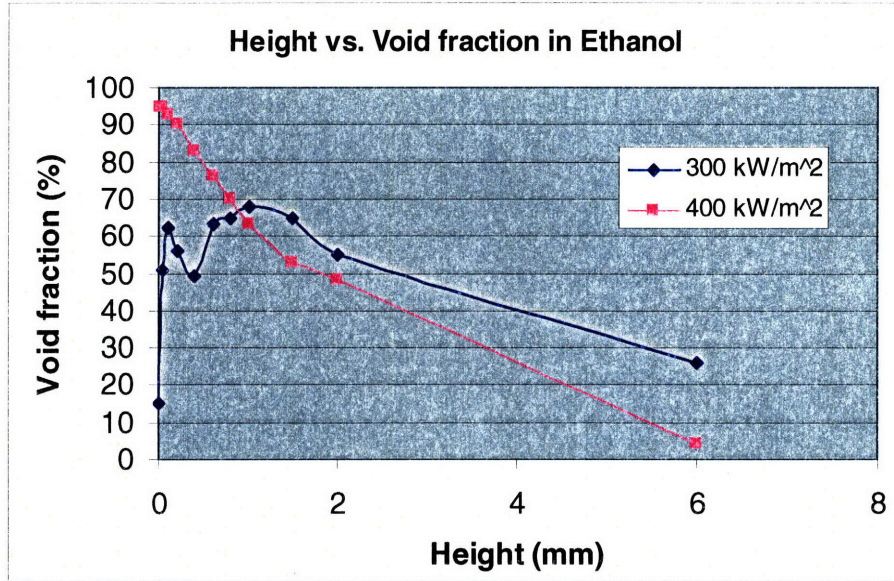
Figure 4-4: Height vs. void fraction in Ethanol during nucleate boiling (300 kW) and film boiling (400 kW)

To determine if the macrolayer does change according to heat flux as in equation (2-8), and if the change in macrolayer is correlated to an increase in CHF as suggested in equation (2-7), several trials need to be performed at various heat fluxes and for different fluids, including nanofluids.

For DI water, three different runs were performed, in which macrolayer measurements were made for 2 different heat fluxes. For these water runs 3 CHF values have been recorded (avg.=1351 kW/m^2, σ=260kW/m^2) as well as a range of heat fluxes from 333 kW/m^2 to 1110 kW/m^2. Shown below is the graph that displays the reduction of the macrolayer with increasing heat flux, along with an increase of the maximum void fraction for higher heat flux.
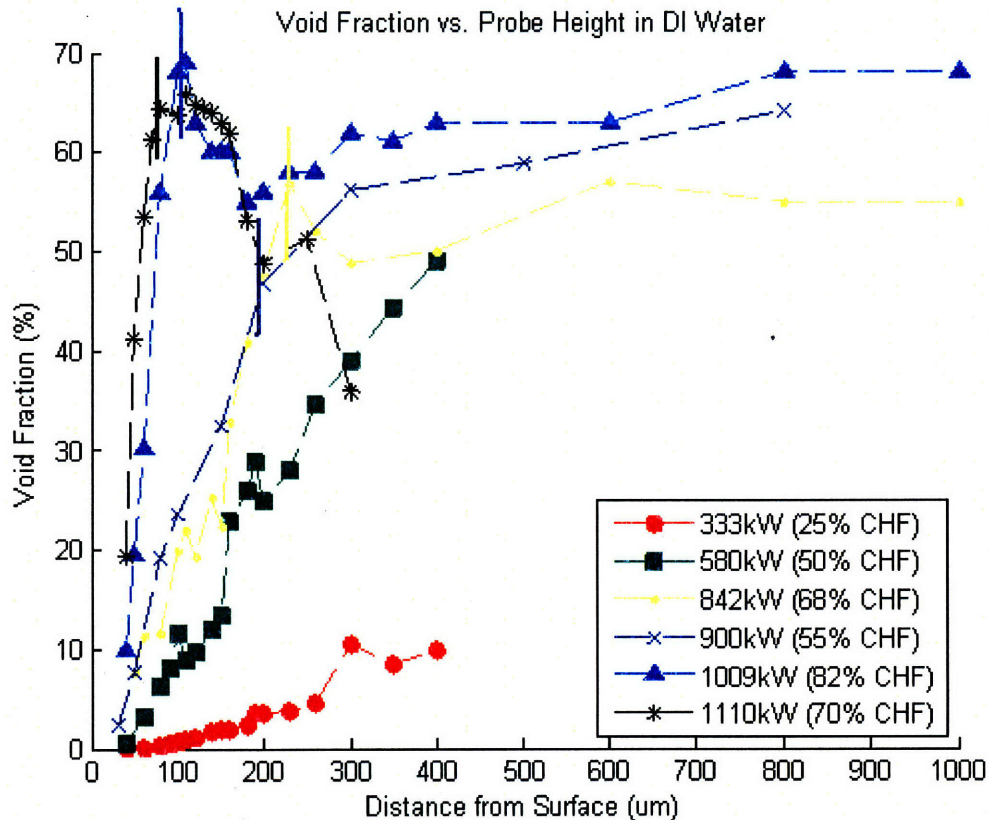
Figure 4-5: Void Fraction vs. height for several heat fluxes in DI

The respective percent of heat flux is given as well as the actual heat flux value (in kW/m^2). The macrolayer thickness is shown for the four highest heat fluxes as a vertical line in the same color its respective heat flux. For the lower heat fluxes, no clear macrolayer exists, as there does not seem to be a maximum void fraction. This liquid layer begins to form as boiling progresses and is quite obvious at high heat fluxes (1009 kW/m^2, 1110 kW/m^2).

For the .01%v Silica, there were two different runs, each producing a CHF value (avg.=2285 kW/m^2, σ=261kW/m²). Unfortunately, the optical probe data from one of the runs was unusable, so on the figure below, all of the data came from the case where CHF=2540 kW/m^2, with the highest heat flux 2126 kW/m^2 being 84% of the CHF value.
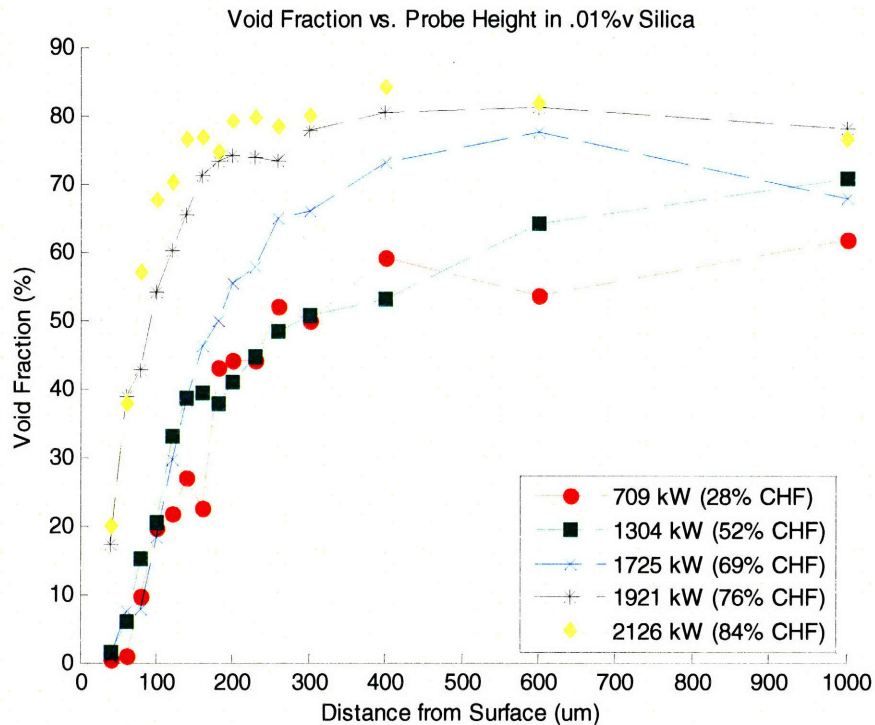
Figure 4-6: Void Fraction vs. height for several heat fluxes in .01%v Silica

Similar to Figure (5-8), this graph shows an increasing void fraction with increasing heat flux as well as a decreasing macrolayer. However, the macrolayer of comparable heat fluxes between the water and silica is very different. For instance, at 1300 kW/m^2 in Silica, no clear macrolayer is established, yet at 1110 kW/m^2 in water, the macrolayer has already shrunk to below 100 µm, and is very close to CHF. Shown below is a table containing all of the macrolayer values for each heat flux.

Table 4-1: List of macrolayer thicknesses for all heat fluxes

Fluid	Heat Flux (kW/m^2)	Macrolayer (um)
	333	N/A
	580	N/A
	842	230
	900	200
	1009	110
DI Water	1110	80
	709	N/A
	1304	N/A
	1725	260
.01%v	1921	190
Silica	2126	140

Using the correlations for macrolayer in a pure substance [22], and in a general fluid (containing a sensitivity to contact angle) [24], the experimental data from the PBE can be compared to the theoretical values of macrolayer. For the theoretical fit, equation 2-8, from [22], all of the parameters are fluid properties that can be found in table 3-2, with the exception of h_{fg}. This value was found in fluid properties table provided by NIST. [38] The values for equation 2-11, the contact angle, and the coefficient c were taken from table 2-1 [21], and [24] respectively. Equation 2-8 does not take into account the change in wettability of a fluid on the macrolayer thickness. At low concentrations of nanoparticles, such as in this experiment, the fluid properties in equation 2-8 do not change very much, so to accurately predict the macrolayer thickness of nanofluids, another model must be used. Equation 2-11 correlates the macrolayer thickness to wettability, so that model will be used to predict the macrolayer in nanofluids. The figure below plots both equation 2-8 and 2-11 with the experimental results from the macrolayer experiments for DI water and .01%v Silica respectively.

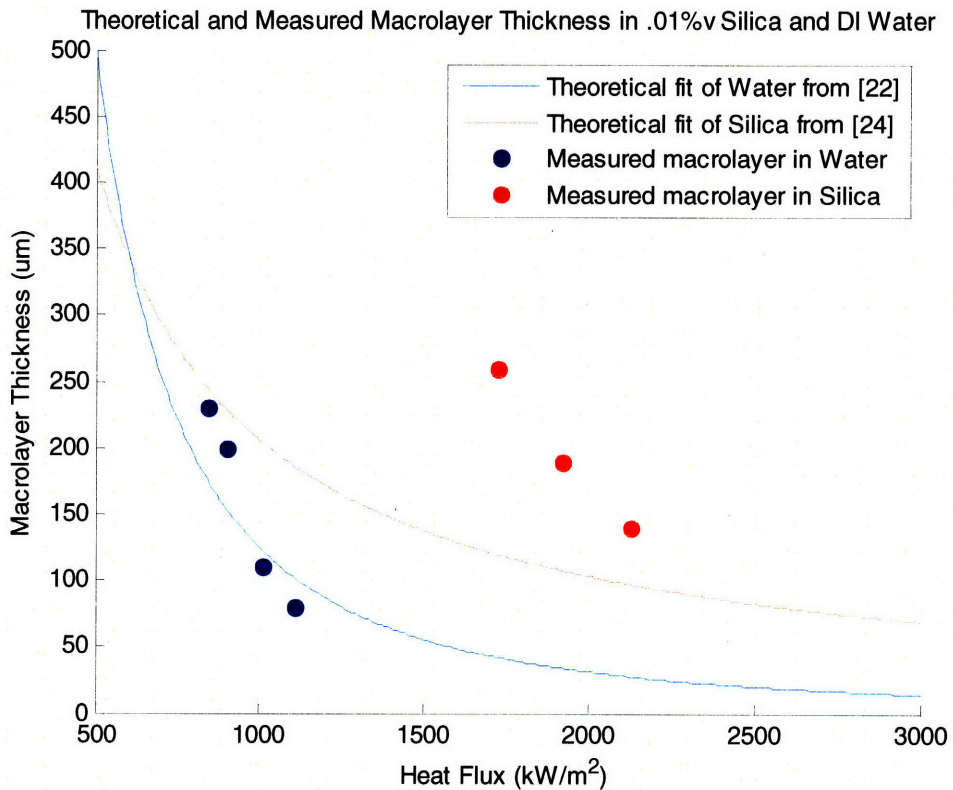Theoretical and Measured Macrolayer Thickness in .01%v Silica and DI Water

Figure 4-7: Theoretical macrolayer thickness in DI water and .01%v silica with the corresponding experimental measurements of macrolayer

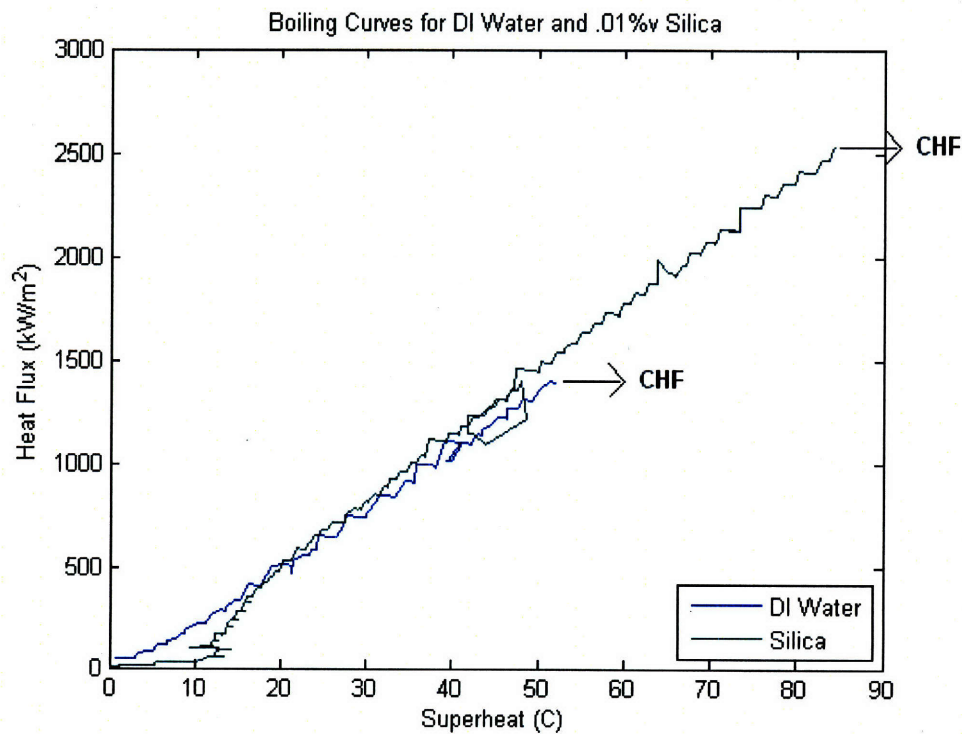Boiling Curves for DI Water and .01%v Silica

Figure 4-8: Boiling curve for DI water and silica

Finally, a boiling curve for each fluid, water and silica (shown above), was recorded using the thermocouple on the bottom of the heater (corrected for conductance through the heater) and the data recorded by the DAQ. The heat flux was calculated by equation 4-1, and then compared to the superheat. When performing a linear fit for the water boiling curve, a heat transfer coefficient h_{water} is calculated to be 28.5 kW/m^2 °C. The heat transfer coefficient for silica h_{silica}=31.2 kW/m^2 °C. This indicates a 9% enhancement in boiling heat transfer as well as an 82% enhancement in CHF.

5   Discussion

5.1   OP verification

The optical probe directly measures only number of bubbles, vapor time, and flight time. These directly measured values are very accurate, which indicates that the values of number of bubbles and void fraction will be accurate enough to be considered without error. The rest of the bubble/fluid parameters are all derived from these three measurements, but with some error. The probe processing software makes some assumptions about the bubbles being measured. Measurements are only made in the vertical direction so in the case of elliptical bubbles the diameter will be calculated only on the minor axis, underestimating the size.

A major goal for this part of the experiment was to obtain spherical bubbles, which would give the probe ideal test conditions. This ended up not being possible because the only spherical bubbles, using glycerin as the fluid, cannot be measured by the probe due to the fluid's high viscosity. Most of the tests ended up using water as the fluid, which is appropriate considering that many of the nanofluids are water based, which produces wobbling bubbles. Even at the lowest flow rates of the flow meter for the air-water validation tests, bubble agglomeration was

common and augmented the tendency of the bubbles to be non-spherical, possibly skewing the probe's measurements and calculations.

5.2   Macrolayer Measurements

The values of CHF measured for water in these experiments are higher than most of the previous reported data. Many of the previous tests have indicated that the CHF for water is somewhere around 1000 kW/m^2, but no higher than 1100-1200 kW/m^2. [20] The higher values in the present experiments come form sandblasting the surface. On the other hand, the nanofluid CHF data from Vassallo et. al. [15] for 0.5% silica are at 3200 kW/m^2 and 2600 kW/m^2, which is higher than the average value measured here for silica nanofluids (2285 kW/m^2); however, Vassallo's silica nanofluids contain a nanoparticle concentration that is 50 times higher.

For the case of the silica nanofluid, the CHF value is also affected by the long boiling time due to the length of the experiment. As the boiling time increases, the nanoparticles are deposited on the heater surface, which increases the wettability of the heater. [21] In the case of figure 4-7, the macrolayer thickness is much larger than the correlation from [24] states that it would be. This large macrolayer is indicative of a higher CHF value. The boiling time for each one of these experiments was several hours due to the large volume of water that needed to be heated as well as the time to take the optical probe measurements. During this time, more nanoparticles may have deposited on the heater surface than normally would. This increases wettability led to a thicker macrolayer, which increased the CHF. The enhancement of .5% silica from [15] was between 60%-100%, whereas the enhancement here was 82% (with much smaller nanoparticle concentration).

The boiling curve of both water and the .01%v silica, figure 5-12, shows the drastic

increase in CHF, but also a very slight change in the heat transfer coefficient. By rearranging

equation 2-1, the heat transfer coefficient can be found by,

$$h = \frac{q''}{\Delta T} = slope \qquad \textbf{(5-1)}$$

This slope is only calculated during nucleate boiling, where the boiling curve becomes linear

(above 200 kW/m^2 for water and 500 kW/m^2 for the silica). At low heat flux, water seems to

have a higher heat transfer coefficient, while at higher heat flux the silica nanofluid has a higher

heat transfer coefficient. The increase in heat transfer coefficient, at this nanoparticle

concentration, comes with virtually no increase in viscosity that would make the pumping power
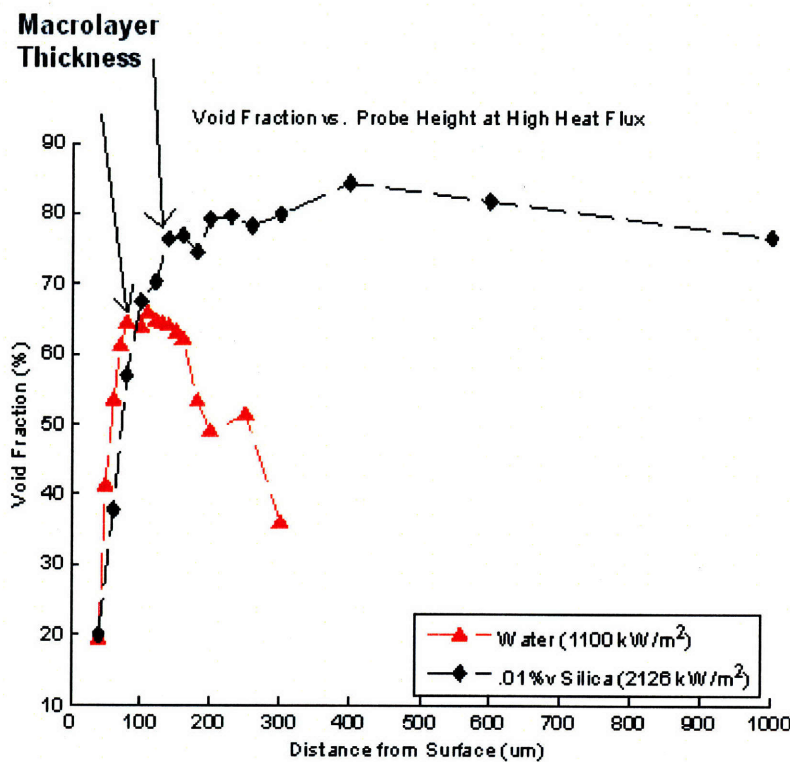
increase. [13]

Figure 5-1: Void fraction vs. height at 80% of CHF

Figure 5-1 shows the effect of nanoparticles on the macrolayer thickness. The void fraction of the silica is much higher due to the higher heat flux, so more evaporation is needed to remove heat from the heater. In addition, the macrolayer is clearly smaller for the water, which could explain the lower CHF value.

6 Conclusion

An experimental study of air bubble parameters in various fluids was conducted by means of an optical probe. Even with the characteristic of wobbling bubbles and spherical caps (R-123), the probe accurately measured the bubble characteristics in accordance with the camera measurements, but higher than the theoretical values, probably because of bubble agglomeration. Overall, the error for diameter is around 10% and the error for velocity is about 5%. These values provide confidence for future use of the probe.

The probe was then used in boiling experiments with pure water and a silica nanofluid. The probe could reproduce the expected trend of increasing void fraction with increasing heat flux. The agreement between the theoretical macrolayer thickness in [19] and [24], and the experimental data from [22], [23], and [25] indicates that the macrolayer is following a correct trend. The enhancement of CHF of silica over water (82% enhancement) can be correlated to the increased size of the macrolayer at high heat flux. The correlation for silica may not be quite accurate, but the high CHF values of silica due to some other factor may have caused the slightly high CHF and macrolayer thickness. Further research could be done by finding the void fraction vs. height for additional nanofluids and measuring bubble parameters in boiling experiments at low heat flux.

References

[1]   OECD. Agency, "Generation IV International Forum 2007 Annual Report."
[2]   DOE, "U.S. Nuclear Plants - Watts Bar," 2004.
[3]   INL, "Generation IV Nuclear Energy Systems," 2007.
[4]   S. K. Das, N. Putra, P. Thiesen, W. Roetzel, "Temperature Dependence of Thermal Conductivity Enhancement for Nanofluids," *Journal of Heat Transfer*, vol. 125, pp. 567-574, 2003.
[5]   S. Maiga, S. Palm, C. Nguyen, G. Roy, N. Galanis, "Heat transfer enhancement by using nanofluids in forced convection flows," *International Journal of Heat and Fluid Flow*, vol. 26, pp. 530-546, 2005.
[6]   S. J. Kim, I. C. Bang, J. Buongirono, L.W. Hu, "Surface wettability change during pool boiling of nanofluids and its effect on critical heat flux," *International Journal of Heat and Mass Transfer*, vol. 50, pp. 4105-4116, 2007.
[7]   S. M. You, J. H. Kim, K. H. Kim, "Effect of nanoparticles on critical heat flux of water in pool boiling heat transfer," *Applied Physics Letters*, vol. 83, pp. 3374-3376, 2003.
[8]   D. Incropera, Bergman, Lavine, *Fundamentals of Heat and Mass Transfer 6th Edition*. Hoboken, NJ: John Wiley & Sons, 2007.
[9]   R. A. Knief, *Nuclear Engineering: Theory and Technology of Commercial Nuclear Power*. Philadelphia: Hemisphere Publishing Company, 1992.
[10]   J. Buongiorno, L.W. Hu, S.J. Kim, R. Hannink, B. Truong, E. Forrest, "Nanofluids for enhanced economics and safety of nuclear reactors: an evaluation of the potenital features, issues, and research gaps," *Nuclear Technology*, vol. 162, pp. 80-91, 2008.
[11]   S. H. Kim, S. R. Choi, and D. Kim, "Thermal Conductivity of Metal-Oxide Nanofluids: Particle Size Dependence and Effect of Laser Irradiation," *Journal of Heat Transfer*, vol. 129, pp. 298-307, 2007.
[12]   J. Buongiorno and B. Truong, "Preliminary Study of Water-Based Nanofluid Coolants in PWRs," in *ANS Annual Meeting*, San Diego, June 5-9, 2005, pp. 383-384.
[13]   R. Prasher, D. Song, J. Wang, and P. Phelan, "Measurements of nanofluid viscosity and its implications for thermal applications," *Applied Physics Letters*, vol. 89, pp. 133108-3, 2006.
[14]   W. Williams, "Experimental and Theoretical Investigation of Transport Phenomena in Nanoparticle Colloids (Nanofluids)," in *Nuclear Science and Engineering*. vol. Ph.D Cambridge: MIT, 2006.
[15]   P. Vassallo, R. Kumar, S. D'Amico, "Pool boiling heat transfer experiments in silica–water nano-fluids," *International Journal of Heat and Mass Transfer*, vol. 47, pp. 407-411, 2003.
[16]   I. C. Bang and S. Heung Chang, "Boiling heat transfer performance and phenomena of Al2O3-water nano-fluids from a plain surface in a pool," *International Journal of Heat and Mass Transfer*, vol. 48, pp. 2407-2419, 2005.
[17]   H. Kim, J. Kim, M.H. Kim, "Effect of nano-particles on CHF enhancement in pool boiling of nano-fluids," *Internation Journal of Heat and Mass Transfer*, vol. 49, pp. 5070-5074, 2006.
[18]   N. Zuber, "Hydrodynamic Aspects of Boiling Heat Transfer," in *Engineering*. vol. Ph.D Los Angeles: UCLA, 1959.

[19]   Y. Haramura, Y. Katto, "A new hydrodynamic model of critical heat flux, applicable widely to pool and forced convection boiling on submerged bodies in saturated liquid," *Internation Journal of Heat and Mass Transfer,* vol. 26, pp. 389-399, 1983.

[20]   I. C. Bang, J. Buongirono, L.W. Hu, H. Wang, "Measurement of Key Pool Boiling Parameters in Nanofluids for Nuclear Applications," in *15th International Conference on Nuclear Engineering* Nagoya, Japan, 2007.

[21]   S. J. Kim, I.C. Bang, J. Buongiorno, L.W. Hu, "Study of pool boiling and critical heat flux enhancement in nanofluids," *Pol. Ac. Tech.,* vol. 55, 2007.

[22]   A. K. Rajvanshi, J.S. Saini, R. Prakash, "Investigation of macrolayer thickness in pool boiling at high heat flux," *International Journal of Heat and Mass Transfer,* vol. 35, pp. 343-350, 1992.

[23]   H. Sakashita, T. Kumada, "Macrolayer Formation and Mechanisms of Nucleate Boiling, Critical Heat Flux, and Transition Boiling," *Heat Transfer - Japanese Research,* vol. 27, pp. 155-168, 1998.

[24]   P. Sadasivan, P. R. Chappidi, C. Unal, and R. A. Nelson, "Possible mechanisms of macrolayer formation," *International Communications in Heat and Mass Transfer,* vol. 19, pp. 801-815, 1992.

[25]   M. Buchholz, T. Luttich, H. Auracher, W. Marquardt, "Experimental investigation of local processes in pool boiling along the entire boiling curve," *International Journal of Heat and Fluid Flow,* vol. 25, pp. 243-261, 2004.

[26]   T. G. Theofanous, T. N. Dinh, J. P. Tu, and A. T. Dinh, "The boiling crisis phenomenon: Part II: dryout dynamics and burnout," *Experimental Thermal and Fluid Science,* vol. 26, pp. 793-810, 2002.

[27]   T. G. Theofanous, J. P. Tu, A. T. Dinh, and T. N. Dinh, "The boiling crisis phenomenon: Part I: nucleation and nucleate boiling heat transfer," *Experimental Thermal and Fluid Science,* vol. 26, pp. 775-792, 2002.

[28]   W. Rosenhow and P. Griffith, "Correlation of maximum heat flux data for boiling of saturated liquids," MIT, Cambridge 1955.

[29]   G. Bekefi, A. Barrett, "Electromagnetic Vibrations, Waves, and Radiation," Cambridge, MA: The MIT Press, 1990, pp. 453-519.

[30]   RBI, "Opto-Electronic Unit."

[31]   RBI, "ISO Software User's Guide: Two Phase Flow Study."

[32]   P. B. Whalley, *Boiling, Condensation, and Gas-Liquid Flow*: Oxford University Press, 1990.

[33]   "Surface tension values of some common test liquids for surface energy analysis," 2006.

[34]   "The Liquid State: Viscosity and Surface Tension of Varoius Liquids at 293 K," 2006.

[35]   "Acetone Solvent Properties," 2006.

[36]   "Ethylene Glycol: Physical Properties," 2008.

[37]   C. Gerardi, "Probe distance calibration," E-mail ed, A. Lerch, Ed., 2008.

[38]   "Thermophysical Properties of Fluid Systems." vol. 2008, NIST, Ed., 2005.